

Biodistribution and Dosimetry Evaluation for A Novel Tau Tracer [18F]-S16 in Healthy Volunteers and Its Application in Assessment of Tau Pathology in Alzheimer's Disease

Ying Wang

Tianjin Medical University General Hospital

Li Cai

Tianjin Medical University General Hospital

Kaixiang Zhou

Beijing Normal University

Mengchao Cui

Beijing Normal University

Shaobo Yao (✉ yaoshaobo008@163.com)

The First Affiliated Hospital of Fujian Medical University <https://orcid.org/0000-0003-2245-871X>

Research Article

Keywords: Radiation dosimetry, Alzheimer's disease, Tau, [18F]-S16, PET/CT

Posted Date: October 19th, 2021

DOI: <https://doi.org/10.21203/rs.3.rs-958599/v1>

License: © ⓘ This work is licensed under a Creative Commons Attribution 4.0 International License.

[Read Full License](#)

Version of Record: A version of this preprint was published at Frontiers in Bioengineering and Biotechnology on February 10th, 2022. See the published version at <https://doi.org/10.3389/fbioe.2021.812818>.

Biodistribution and Dosimetry Evaluation for A Novel Tau Tracer [¹⁸F]-S16 in Healthy Volunteers and Its Application in Assessment of Tau Pathology in Alzheimer's Disease

Authors: Ying Wang^{1*}, Li Cai¹, Kaixiang Zhou², Mengchao Cui², Shaobo Yao^{1,3†}

¹ Department of PET/CT Diagnostic, Tianjin Medical University General Hospital, Tianjin, 300052, China

² Key Laboratory of Radiopharmaceuticals, Ministry of Education, Beijing Normal University, Beijing, 100875, China

³ Department of Nuclear Medicine, Fujian Provincial Key Laboratory of Precision Medicine for Cancer, The First Affiliated Hospital of Fujian Medical University, Fuzhou, Fujian, 350005, China

†Corresponding authors:

Shaobo Yao, PhD

Address: No.154, Anshan Road, Heping District, Tianjin, 300052, China

Tel.: +86 02260362190 Fax: +86 02260362195

E-mail: yaoshaobo008@163.com.

***First authors:**

Ying Wang, M.D.

Address: No.154, Anshan Road, Heping District, Tianjin, 300052, China

Tel.: +86 02260362190 Fax: +86 02260362195

E-mail: macrossplusvoices@163.com

The word count of the manuscript: 6049 words.

Funding: This study was funded in part by the National Natural Science Foundation of China 82171982. Natural Science Foundation of Fujian 2020J05249. Fujian Provincial Health Commission Science and Technology and Programme 2020GGA045. Tianjin Education Commission Scientific Research Project 2018KJ060

Running title: Clinical evaluation of [¹⁸F]-S16

ABSTRACT

Background: The goal of this study was to report a fully automated radiosynthetic procedure of a novel tau tracer [^{18}F]-S16 and its safety, biodistribution and dosimetry evaluation in healthy volunteers. And the potential utility of [^{18}F]-S16 PET imaging in AD tauopathies, as well as to identify the relationship between cerebral tau pathology and hypometabolism patterns using both [^{18}F]-S16 and [^{18}F]-FDG were also discussed.

Methods: The automated radiosynthesis of [^{18}F]-S16 was performed on a GE Tracerlab FX2 N module, and the in vitro stability was evaluated. For the biodistribution and radiation dosimetry study, healthy volunteers were underwent a series PET scans acquired at 10, 60, 120 and 240min post-injection. The biodistribution in normal organs and safety were assessed. Radiation dosimetry was calculated using OLINDA/EXM 1.0. For AD diagnosis study, participants with a clinical diagnosis of probable AD and healthy controls (HCs) underwent dynamic [^{18}F]-S16 and static [^{18}F]-FDG PET imaging. [^{18}F]-S16 binding was assessed visually and quantitatively using SUV ratios (SUVRs) measured at different regions of interests (ROIs), with the cerebellar cortex as the reference region. SUVRs of [^{18}F]-FDG in 10 min static data were calculated using mean activity in the pons as the reference region. [^{18}F]-S16 SUVRs were compared between the AD and HCs in different ROIs using the Mann-Whitney U test. In AD patients with all cortical ROI regions, Spearman rank correlation analysis was used to calculate the voxel-wise correlations between [^{18}F]-S16 PET and [^{18}F]-FDG.

Results: The automated radiosynthesis of [^{18}F]-S16 was finished within 45 min, with a radiochemical yield (RCY) of $30 \pm 5\%$ ($n = 8$, non-decay-corrected). The radiochemical purity (RCP) was greater than 98% and the specific activity (SA) was calculated to be $1047 \pm 450 \text{ GBq}/\mu\text{mol}$ ($n = 5$), and [^{18}F]-S16 was stable in vitro. In the pilot volunteer study, no adverse effects caused by [^{18}F]-S16 was observed within 24 hours post-injection and no defluorination was observed in vivo. The radiotracer could pass through the blood-brain barrier (BBB) easily, and rapidly cleared from the circulation and excreted mainly through the hepatic system. The absorbed dose of the urinary bladder wall was the highest, $133.7 \pm 60.9 \mu\text{Sv}/\text{MBq}$. The whole-body mean

effective dose was $15.3 \pm 0.3 \mu\text{Sv/MBq}$. In AD subjects, [^{18}F]-S16 accumulation was identified in cortical regions mainly involving parietal, temporal, precuneus, posterior cingulate and frontal lobes. No specific [^{18}F]-S16 cerebral uptake region was identified visually in HCs. SUVR of AD subjects in these regions was significantly higher than that of HCs. Tracer retention was observed in the substantia nigra and brainstem of both AD subjects and HCs. No specific binding uptake compared with reference region was found in the choroid plexus, venous sinus and white matter. A significant correlation was found between [^{18}F]-S16 binding and hypometabolism across neocortical regions.

Conclusion: [^{18}F]-S16 could be synthesized automatically and it showed favorable biodistribution and safety in human. The dosimetric parameters were safe and comparable to other tau tracers. [^{18}F]-S16 PET indicated a high image quality for imaging tau deposition in AD subjects, and distinguishing AD from HCs.

Keywords: Radiation dosimetry; Alzheimer's disease; Tau; [^{18}F]-S16; PET/CT

Introduction

Alzheimer's disease (AD) is a progressive, neurodegenerative condition that results in both cognitive and functional decline. The enormous human and socioeconomic burden associated with AD has motivated an intense international research effort directed toward earlier and more accurate diagnosis and the development of disease-modifying treatments. Amyloid- β ($A\beta$) plaques, together with tau neurofibrillary tangles (NFTs), are the neuropathological hallmarks of AD [1]. It has been proposed to classify AD according to the biomarkers for amyloid, tau and neuronal injury by the A/T/N scheme [2]. The correlations among amyloid accumulation, neurodegeneration and clinical decline are not straightforward. Conversely, the distribution and burden of NFTs shows a closer association with neurodegeneration and clinical status [3].

Tau is a complex protein with multiple isoforms and post-translational modifications. Tracers may bind to specific or multiple isoforms. As tau is an intracellular protein, radioligands must cross the cell membrane of neurons. In addition, $A\beta$ and tau both manifest β -sheet structure which binds planar polyaromatic ligands. A selective ligand needs to have at least 10-fold higher binding affinity for tau compared with $A\beta$ [4]. In recent ten years, a number of tau ligands for in vivo positron emission tomography (PET) imaging have been developed and evaluated in both preclinical and clinical studies. Tau-PET imaging has opened a unique window to expand our insight into the pathology of AD and other tau related neurodegenerative diseases. Representative tau-PET ligands including the first generation tracers, THK tracers, T807/T808 and [^{11}C]-PBB3, and the second generation tracers, [^{18}F]-MK-6240, [^{18}F]-APN-1607, and [^{18}F]-PI-2620 can reflect the timing and distribution of tau in the early phases of neurodegenerative diseases [5-9].

However, almost all of the first generation tau tracers mentioned above presented the same drawback, various degrees of what has been called "off-target" binding. This means the retention of radiotracers in the brain areas without tau deposition, such as the basal ganglia, the choroid plexus, or the thalamus [6-7]. In addition, the THK

tracers, including [^{18}F]-THK523, [^{18}F]-THK5317 and [^{18}F]-THK5351 displayed some white matter retention which hindered accurate visual interpretation of signals [10,11]. [^{18}F]-T808 showed high binding affinity and good selectivity for tau over A β and with rapid uptake and washout in transgenic mice, however, high defluorination in vivo hindered its further development and application in clinical studies [8]. Drawbacks of [^{11}C]-PBB3 include its short half-life requiring on-site synthesis and the formation of cis-trans isomers under the light during the radiosynthesis [12-14]. Initial human studies of some second-generation tracers such as [^{18}F]-MK6240 have shown no “off-target” binding so far, however, further detailed clinical trials were still needed [15].

We had developed a novel tau PET radiotracer [^{18}F]-S16 ([^{18}F]-(*S*)-1-(4-(6-(dimethylamino)quinoxalin-2-yl)phenoxy)-3-fluoropropan-2-ol) with a 2-phenylquinoxaline scaffold. [^{18}F]-S16 displayed high affinity and selectivity for tangles over A β , as well as sufficient BBB penetration and rapid brain washout in normal mice [16]. The goal of this study was to report a fully automated radiosynthetic procedure of [^{18}F]-S16 and to evaluate its safety, biodistribution and dosimetry in healthy volunteers. Moreover, we aimed to identify the [^{18}F]-S16 binding patterns in AD relative to sex- and age-matched healthy controls (HCs), and the relationship between cerebral tau pathology and hypometabolism patterns with dual [^{18}F]-S16 (T) and [^{18}F]-FDG (N). The flowchart of study design was in [Supplemental Materials \(SM\) Fig. S1](#).

Materials and methods

General

All chemicals obtained commercially were of analytical grade (Sigma-Aldrich, USA) and used without further purification otherwise stated. The tosylate precursor and [^{19}F]-labeled reference ligand were supplied by Prof. Cui. Sep-Pak light QMA and Sep-Pak plus (light) C18 cartridges were obtained from Waters (Milford, USA). Sep-Pak light QMA cartridges were pre-conditioned with 8.4% NaHCO₃ (8 mL)

and water (10 mL) before use. Sep-Pak C18 plus cartridges were preconditioned with ethanol (10 mL) and water (10 mL) in advance. Fetal bovine serum was purchased from HyClone (Thermo Scientific, USA) and stored under -20 °C before use.

Automated Radiosynthesis of [¹⁸F]-S16

[¹⁸F]-S16 was prepared by a one-pot two-step reaction described in [SM Fig. S2](#). The automated radiosynthesis of [¹⁸F]-S16 was performed on the GE Tracerlab FX2 N synthesis unit (GE Healthcare, USA). No-carrier-added [¹⁸F]-fluoride was produced through the nuclear reaction ¹⁸O(p, n)¹⁸F by irradiation of more than 95 % [¹⁸O]enriched water target with 10 MeV proton beam on the GE MINItace cyclotron. Millexs-GV 0.22 µm filters units were purchased from Merck Milipore Ltd. The analysis radio-HPLC system was equipped with a gamma ray radiodetector and a UV detector [Varian system: Waters Symmetry C18 column (5 µm, 4.6×250 mm); mobile phase: 1 mL/min with an eluent of CH₃CN/H₂O 50/50]. Radioactivity was measured by a CRC-15PET Radioisotope Dose Calibrator (Capintec, Inc, USA).

Before the reaction, Vial 1 was filled with a mixture of Kryptofix 222 (K₂₂₂, 13 mg), potassium carbonate (K₂CO₃, 1.1 mg), CH₃CN (0.3 mL) and H₂O (0.3 mL); vial 2 was filled with anhydrous CH₃CN (1 mL); vial 3 was filled with compound **1** (3 mg) dissolved in anhydrous CH₃CN (1.5 mL); vial 4 was filled with 0.5 M HCl (0.5 mL); vial 5 was filled with 0.5 M NaOH (0.5 mL); vial 6 was filled with 2.5 mL CH₃CN/H₂O (60/40) mixture; vial 12 was filled with saline (10 mL); vial 13 was filled with ethanol (1 mL); vial 14 was filled with H₂O (10 mL); the round bubble vessel at the right bottom was filled with 50 mL H₂O.

After [¹⁸F]-fluoride (800-1000 mCi) was delivered from the cyclotron and trapped on QMA, the excess ¹⁸H₂O was removed. The trapped [¹⁸F]activity was eluted to the reactor 1 with K₂₂₂ elution (0.6 mL, vial 1). The reaction mixture was evaporated under a stream of nitrogen (80 mL/min) at 95°C under reduced pressure. The residue was azeotropically dried with CH₃CN (1 mL, vial 2) at 95°C again. Then a solution of compound **1** (3 mg) in anhydrous CH₃CN (1.5 mL, vial 3) was added and the fluorination was carried out at 100°C for 5 min. The reaction mixture was bubbled

with N₂ to dryness, HCl solution (0.5 mL, vial 4) was added to the reaction vessel and heated at 100°C for 3 min. After adding NaOH solution (0.5 mL, vial 5) and mixture of CH₃CN and H₂O (2.5 mL, vial 6), the mixture was loaded to the semi-prep HPLC system (Sykm S1122 Solvent Delivery System) equipped with a gamma ray radiodetector and a UV detector [Machery-Nagel Nucleosil 100-7 C18 column (16×250 mm); mobile phase: 16 mL/min with an eluent of CH₃CN/H₂O 60/40]. After the collection of product gradient, the elution was diluted with H₂O (50 mL) in the bubble vessel and transferred to the C18 cartridge. The C18 cartridge was washed with H₂O (10 mL, vial 14) to remove high polarity impurities and dried with Helium. The radioactivity was eluted by ethanol (1 mL, vial 13) and diluted by saline (10 mL, vial 12). [¹⁸F]-S16 saline was filtered through a sterile Millipore GV filter (0.22 μm, 25 mm) directly into a sterile product vial (20 mL size).

Chemical identification of the purified product was carried out by HPLC co-injection with the non-radioactive reference [¹⁹F]-S16, using UV detector at 254 nm and a gamma ray radiodetector. The analysis radio-HPLC condition was the same as mentioned above.

For in vitro assays, 0.1 mL samples of [¹⁸F]-S16 (1.85 MBq, 50 μCi) were dissolved in sterile saline and incubated with 0.2 mL of fetal bovine serum (FBS) at 37 °C with gentle shaking. An aliquot of the injection saline and the serum sample was analyzed by radio-HPLC to determine the percentage of intact [¹⁸F]-S16 at 120 min.

Participants and Methods

Clinical study was approved by the Institute Review Boards of Tianjin Medical University General Hospital (TMUGH) (IRB2018-072-01). Participant recruitment and the clinical trial were conducted from Aug 10, 2018 to Aug 10, 2020. The trial was registered on Clinicaltrial.gov with the identified number of NCT03620552.

In pilot study, four healthy volunteers with the age of 49.25 ± 11.52 (3 men and 1 woman, MMSE 30) were enrolled in the study after obtaining written informed consent. These subjects were deemed to be in good health based on their clinical

history, physical examination, standard blood and urine tests, and electrocardiogram. Subjects were contacted by telephone approximately 24h after [¹⁸F]-S16 administration to monitor adverse events.

In AD diagnosis study, fifteen probable AD patients and six ageand sexmatched HCs were recruited from research cohorts of the Department of Neurology. They all received a standard clinical evaluation, including a comprehensive neurological history, physical and neurological examinations (brain MRI and neuropsychological assessment with a battery of tests). All the subjects were Han Chinese. Clinical diagnosis was determined by consensus of a multidisciplinary team. The diagnosis of probable AD was based on the NINCDS/ADRDA and DSM-IV criteria. At screening, a Clinical Dementia Rating (CDR) score was at least 0.5, and a Mini-Mental State Examination (MMSE) score was no more than 28. They all had positive [¹¹C]-Pittsburgh compound B ([¹¹C]-PiB) PET scan (assessing in vivo amyloid pathology) under the published procedures[17]. The inclusion criteria for HCs were no history of major psychiatric or neurological illnesses, head injury, no family history of AD. A MMSE score was more than 28 and a CDR score was 0. The HCs had negative [¹¹C]-PiB PET scans. All participants (or their legal representatives) provided written informed consent to participate in the study. Demographics and clinical data were summarized in [SM Table 1](#).

[¹⁸F]-S16 and [¹⁸F]-FDG PET/CT

In the pilot study, four healthy volunteers underwent a total of 4 sequential whole-body [¹⁸F]-S16 PET/CT scans from base of the skull to proximal thigh using Discovery PET/CT 710 scanner (GE Healthcare, Milwaukee, WI, USA). The [¹⁸F]-S16 radiotracer was injected through a venous line into the arm of healthy volunteers with a mean administered activity of 444 ± 37 MBq. The radiotracers were administered to subjects by rapid bolus injection (5 mL over 15 seconds). The low-dose CT scan of each subject for locating and attenuation correction was obtained from base of the skull to proximate thigh (CT settings: 120 KeV; 30mAs; pitch, 0.984; slice thickness, 3.75 mm; rotation time, 0.8 s). The scanning protocol included 2 min

emission scans for four cycles at 10, 60, 120, and 240min post-injection. Each cycle consisted of eight bed positions, thus the whole-body scanning time was 16 min per cycle. A ten minutes static brain scan was also performed following the second whole-body scan approximately 76 minutes after injection. All data were decay corrected to the starting time of each individual scan. All PET images were corrected for photon attenuation, dead time, random events, and scatter. Images were reconstructed in the three-dimensional mode using an OSEM + PSF + TOF reconstruction technique (ordered-subset expectation maximization with 24 subsets and two iterations). The image matrix was 256×256 (pixel size, 2.73 mm) and slice thickness was 3.27 mm.

In AD diagnosis study, each subject completed [^{18}F]-S16 and [^{18}F]-FDG PET scans within one week. Participants with intravenous injection of [^{18}F]-S16 (383.6 ± 30.6 MBq) participated in an acquisition scheme: 70-100 min (5 frames: 6×300 s). A few days later, after fasted for at least 6 hours participants were injected with about 259 MBq [^{18}F]-FDG, a 10 min static PET scans were acquired 40 min post-injection. Each frame produced 35 slices of 4.25 mm thickness, which covered the whole brain. Images were reconstructed to 128×128 matrix (pixel size of 2.5×2.5 mm²).

Safety, Biodistribution and Radiation Dosimetry

Safety and tolerability were assessed including blood and urine samples for laboratory tests, electrocardiograms, physical and clinical examinations. Adverse events were assessed by telephone approximately 24 h after examination. Whole organ volumes of interest were drawn manually over the source organs, including spleen, liver, kidneys, pituitary glands, vertebral bodies L1-L5, and urinary bladder at each time point. The non-decay corrected activities at different time points were documented as percentage of injected dosage and fitted with mono-exponential curves. The area under the time-activity curve between time 0 and the first time point was calculated assuming a linear increase from 0 to the first measured activity. The area under the time-activity curve after the first time point was calculated by trapezoidal integration from the first time point to the last time point and extrapolation from the

last data point using the fitted mono-exponential function. For bone marrow, the residence time was derived by an image-based integration of L1-L5 vertebrae, assuming L1-L5 with 12.3% of the whole-body bone marrow. The urinary bladder residence time was determined by using the voiding bladder model implemented in OLINDA/EXM software, setting a 2-h bladder-voiding interval. The residence time of the rest of the body was calculated as the maximum possible residence time (based on physical decay only) minus the sum of the residence time of all source organs. Absorbed dose of target organs and whole-body effective dose were measured with OLINDA/EXM software by adult male models.

Region of Interest Analyses for [^{18}F]-S16

In the pilot study, three experienced nuclear medicine physicians read all of the images through consensus reading. The same nuclear medicine physician examined and measured the semiquantitative values for the final analysis. GE MMWP workstation was used for postprocessing. The physiologic uptake of the following organs was evaluated at all time points: brain, salivary gland, heart, liver, spleen, bone marrow, kidneys, urinary bladder and small intestine. Regions of interest were drawn over these organs to exclude focal lesions and the maximum standardized uptake value (SUV_{max}) and mean standardized uptake value (SUV_{mean}) normalized to patients' body weight were recorded.

In the AD diagnosis study, images were analyzed in the software package PMOD (version 3.7, PMOD Technologies Ltd., Zurich, Switzerland). Dynamic [^{18}F]-S16 images were coregistered to the standard Montreal Neurologic Institute (MNI) space by applying the 70-100 min transformation (brain normalization settings: nonlinear warping, 8-mm input smoothing, 16 iterations, frequency cut-off 3, regularization 1.0, no thresholding). All images were analyzed in MNI space. A total number of nine predefined regions of interest (ROIs) deriving from the Hammers atlas [\[24\]](#) were delineated in the MNI space, including frontal (superior and middle gyri and orbitofrontal cortex), lateral temporal (superior, middle and inferior gyri), parietal (inferior, superior and supramarginal gyri), occipital (calcarine, cuneus and lateral

occipital cortex), posterior cingulate and precuneus (PCCPRE), medial temporal (entorhinal cortex, hippocampus and parahippocampus, MTL), lentiform (putamen and pallidum), thalamus and white matter (WM). Mean standardized uptake value ratios (SUVRs) of [^{18}F]-S16 were calculated by using mean activity in the cerebellar gray matter as the reference region. These regions were selected as we aimed to assess the full spectrum of Braak stages.

For [^{18}F]-S16 non-displaceable binding potential (BP_{ND}), a measure of specific binding, was determined for each Hammers atlas region of interest using a basis function implementation of the simplified reference tissue model (SRTM) operating upon the hammers atlas and reference tissue ROIs data. Dynamic 70-100 min [^{18}F]-S16 data were analyzed using the non-invasive Logan graphical analysis ($k_2' = 0.05 \text{ min}^{-1}$, $t^* = 80 \text{ min}$), which were used to determine directly BP_{ND} using the cerebellar gray matter as the reference region.

Region of Interest Analyses for [^{18}F]-FDG PET

Mean SUVRs of [^{18}F]-FDG were calculated for 10 min static data by using mean activity in the pons as the reference region. SUVs were calculated by normalizing the uptake values by the injected dose divided by the subject weight. Target-to-pons SUVs were calculated for 10 min static data and compared with [^{18}F]-S16 SUVs.

Statistical Analysis

The comparison of demographic between AD and HCs groups were performed by one-way analysis of variance across groups and Fisher's exact test. [^{18}F]-S16 SUVR data were compared between the AD and HCs groups in different ROIs using the Mann-Whitney U test. In AD patients with all cortical ROI regions, Spearman rank correlation analysis was used to calculate the voxel-wise correlations between [^{18}F]-S16 and [^{18}F]-FDG PET. A significance level of $p < 0.05$ was applied in all analyses. All statistical analyses were performed using SPSS (version 25.0, IBM, Armonk, New York, USA).

Results

Automated Radioynthesis of [^{18}F]-S16

[^{18}F]-S16 was synthesized in 45 mins with a high RCY of $30 \pm 5\%$ ($n = 8$, non-decay-corrected). The identity of [^{18}F]-S16 was confirmed by co-injection of [^{19}F]-S16 as a standard (SM Fig. S3A&B). The radiochemical purity of [^{18}F]-S16 injection was greater than 98% and the specific activity was $1047 \pm 450 \text{ GBq}/\mu\text{mol}$ ($n = 5$) (SM Fig. S4). [^{18}F]-S16 showed high in vitro stability in FBS and saline, and more than 93% and 96% of [^{18}F]-S16 remained intact within 120 min (longer times were tested) (SM Fig. S3C&D).

Safety and Biodistribution

[^{18}F]-S16 was found to be safe and well-tolerated in all subjects. No adverse effects due of [^{18}F]-S16 administration were observed in healthy volunteers up to 24 h after injection. The radiotracer was cleared mainly from the circulation and excreted into the gut through the hepatic-biliary system. The whole body maximum intensity projection (MIP) images of [^{18}F]-S16 at 4 different time points (10-26, 60-76, 120-136 and 240-256 min) post-injection in a healthy volunteer were presented in Fig. 1A. The probe was initially detected in vascular compartment, then rapidly distributed through extracellular space, and finally excreted through the liver, gall bladder (marked with red arrows), colon and small intestine (Fig. 1B&C). Consistent with the hydrophobic characteristic of [^{18}F]-S16 (log P value of 2.61 ± 0.05 , reported in previous paper), it was observed that [^{18}F]-S16 accumulated significantly in liver (hepatic system) but not in kidney (renal system). Moderate uptake was observed in the spleen, heart, brain, parotid gland and salivary gland. Low radioactivity uptake was observed in lungs, pancreas, muscles, bone marrow, which indicates high anti defluorination stability in vivo. The quantitative biodistribution (SUV_{max} and SUV_{mean}) in main organs of healthy volunteers is summarized in Fig. 1G&H. Static brain PET images was presented in Fig. 1D-F, presented as a transverse, coronal, and sagittal plane which were obtained following the second whole-body scanning at 76 min

post-injection. No obvious radioactive uptake was found in cerebral cortex, choroid and sagittal sinus. Moderate radioactivity uptake was observed mainly in bilateral striatum, thalamus, brainstem at 10 min post-injection, then decreased rapidly from 60 to 120 min, and was cleared from the blood pool at 240 min. Brain clearance rate including neocortex, white matter, striatum, thalamus, pons and cerebellum was higher in 60, 120 and 240 min (**Fig. 1I**). The uptake ratio of white matter/neocortex and white matter/striatum increased higher during 10, 60, 120 and 240 min (**Fig. 1H**).

Radiation Dosimetry

The absorbed radiation doses of target organs are summarized in **Table 1**. Gallbladder wall received the highest radiation dose, $133.7 \pm 60.9 \mu\text{Sv/MBq}$. The effective dose was $15.3 \pm 0.3 \mu\text{Sv/MBq}$. The radioactivity uptake of hematopoietic system and genital system was low which also proved its safety.

[¹⁸F]-S16 Visual Assessment

The demographic and clinical characteristics of 15 AD subjects and 6 HCs were summarized in **SM Table S1**. In HCs, no areas of specific [¹⁸F]-S16 cerebral uptake were identified visually (**Fig. 2**), and a consistent pattern of initial uptake and washout was observed. In AD subjects, tracer accumulation was identified in cortical regions mainly involving the parietal and temporal lobes, precuneus, occipital lobes, and frontal lobes. One AD patient (subject#8), revealed with some PCA syndromes, showed significant higher [¹⁸F]-S16 retention in the occipital lobe. Radiotracer retention was observed in the substantia nigra and brainstem of both HCs and AD subjects. No binding higher than the uptake in the reference region was found in the choroid plexus, venous sinus and white matter.

¹⁸F-S16 Binding Related to Clinical Diagnosis and Quantitative Analyses

A comparison of a representative AD and HC subject in the mean [¹⁸F]-S16 BP_{ND} PET map is shown in **Fig. 3A&B**. [¹⁸F]-S16 accumulation in AD subject#6 was identified in cortical regions mainly involving the parietal, temporal, precuneus and frontal lobes. No areas of specific [¹⁸F]-S16 cerebral uptake were identified visually

in HC subject#16. [^{18}F]-S16 retention was observed in the substantia nigra and brainstem of both AD and HC subjects.

ROI analysis of SUVRs were summarized in [Table 2](#). SUVRs of AD ranged from 1.12 to 1.87 (white matter and lentiform, respectively). The lentiform, thalamus, and medial temporal lobe showed the greatest SUVRs in AD. Without the substantia nigra ROIs, the highest SUVRs in AD were the medial temporal lobe (1.59), followed by posterior cingulate and precuneus (1.35), parietal (1.35) and temporal lobe (1.33). SUVRs for HC ranged from 1.01 (white matter) to 1.96 (thalamus). The lentiform, thalamus, and medial temporal lobe also presented with the highest SUVRs in HC. Regions with the lowest SUVR in both AD and HC groups were the white matter. All ROIs had SUVRs were greater than 1.0, indicating that the uptake of [^{18}F]-S16 was greater than that of the cerebellar reference region.

[^{18}F]-S16 uptake in different ROI regions of AD and HC subjects were shown as SUVR box plots in [Fig. 3C](#). AD subjects showed generally higher SUVRs than HC in cortical regions, especially in parietal lobe ($p < 0.0001$), posterior cingulate and precuneus ($p < 0.001$), lateral temporal and occipital lobes ($p < 0.01$), and frontal lobe ($p < 0.05$). However, there was no statistically significant difference in the medial temporal lobe. SUVR analyses of subcortical regions did not show statistically significant differences between AD and HC subjects in thalamus and white matter. However, lentiform revealed significant difference between AD and HCs ($p < 0.05$).

[^{18}F]-S16 Quantitative Analyses and Correlation with Glucose Metabolism

The SUVR values of the summed [^{18}F]-S16 PET and [^{18}F]-FDG PET image were related to all six cortical regions to investigate the regional relationship between tau deposition and glucose metabolism. Spearman rank correlation coefficient (r) was compared between [^{18}F]-S16 PET and [^{18}F]-FDG PET for all cortical ROI regions in AD patients. Correlation coefficients determined by comparing [^{18}F]-S16 SUVR and [^{18}F]-FDG SUVR (global mean and normalization). Correlation plots of [^{18}F]-S16 PET and [^{18}F]-FDG PET were shown in [Fig. 4](#). There was significant difference in the

correlation coefficients between [^{18}F]-S16 and [^{18}F]-FDG PET ($r = -0.44$, $p < 0.0001$) for global mean normalization.

Discussion

In this study, we have reported the fully automated radiosynthesis and the first human PET study of [^{18}F]-S16. No radioactivity uptake in the bone of healthy volunteers guaranteed its stability in vivo. In addition, suitable lipophilicity and molecular weight of [^{18}F]-S16 resulted in their excellent characteristics of crossing the blood-brain-barrier. The biodistribution of [^{18}F]-S16 in humans was consistent with that of animal studies as previously reported. The line of activity seen in [Fig. 1A](#) is tracer accumulation in the vein, which is obvious soon after injection but gradually disappears. The bladder did not show intensive uptake throughout the study. As a result, we deduced [^{18}F]-S16 was mainly excreted through the hepatic-biliary system, resulting in high accumulation in liver and gall bladder. Radioactivity uptake in gall bladder, colon and small intestine increased rapidly, while the kidneys and bladder decreased sharply. The time-distribution pattern of [^{18}F]-S16 in the gall bladder was shown in [Fig. 1B](#) (marked with red arrows). The uptake in gall bladder was low at 10 min post-injection, and it increased to a high level at 60 and 120 min when the probe was gradually secreted into the gall bladder cavity. At 240 min post-injection, the probe was almost fully secreted into gall bladder.

The effective dose of [^{18}F]-S16 was $15.3 \pm 0.3 \mu\text{Sv/MBq}$, which is in the typical range for F-18 radioligand [\[18\]](#). The dosimetry data of [^{18}F]-S16 showed slightly lower effective dose compared to that of other tau tracers ($22.5 \pm 3.6 \mu\text{Sv/MBq}$ for [^{18}F]-AV1451, $22.7 \pm 1.3 \mu\text{Sv/MBq}$ for [^{18}F]-THK5351 and $29.4 \pm 0.6 \mu\text{Sv/MBq}$ for [^{18}F]-MK6240) [\[19-21\]](#).

The present study showed accumulation of [^{18}F]-S16 in regions known to have tau deposition in A β -positive clinically probable AD subjects. HC subjects showed very low [^{18}F]-S16 accumulation in all cortical brain regions, and AD subjects could be clearly distinguished. In the AD group, all cortical ROI regions revealed average SUVR values over 1.19, especially in significant brain areas of the medial temporal

lobe, posterior cingulate and precuneus, parietal lobe, lateral temporal, frontal lobe and occipital lobes associated with tau deposition [22]. The highest uptake of [^{18}F]-S16 was observed in the medial temporal lobe (MTL, including entorhinal cortex, hippocampus and parahippocampus). Higher uptake of [^{18}F]-S16 were observed in posterior cingulate and precuneus, lateral temporal and parietal lobe. The spatial distribution observed here parallels neuropathologic data reporting tau spread from the entorhinal cortex through the inferior-lateral temporal and medial parietal areas to the neocortex[23]. The distribution and density of tracer uptake in AD subjects observed in this study is also consistent with previous tau PET imaging studies[24,25]. Besides, the present study revealed that tracer binding predominantly occurred in the grey matter of AD group. The white matter showed the lowest uptake of [^{18}F]-S16 both in AD and HC groups. High grey-to-white matter ratios in the AD cases reflect radiotracer binding to the cortical neurons that are most affected, and are in good agreement with the excellent contrast observed in human PET scans.

The uptake of [^{18}F]-S16 was significant in the MTL of HCs, which was consistent with previous reported tau tracers. Tau imaging in cognitively normal elderly individuals using [^{18}F]-THK series and [^{18}F]-AV1451, showed radioactivity retention in MTL[26,27]. This pattern of MTL binding is consistent with the neuropathological literature [28]and may reflect an age-related process of tau accumulation in this region [29]so-called primary age-related tauopathy[30]which has been shown to result in hippocampal atrophy and mild amnesic deficits that are amyloid- β -independent [31]. The age-related accumulation of tau, followed by spreading of tau potentiated by A β , disrupts functional memory circuits by disconnecting key MTL structures. Tau pathology plays a role in disconnecting the hippocampus from specific MTL memory systems leading to increased local coherence and memory decline [32].

In this study, we found that one AD patient showed significant higher tracer retention in the occipital lobe (subject#8). This patient revealed PCA syndromes. PCA is a focal neurodegenerative disorder of higher visual processing and spatial praxis with relative sparing of memory and insight, which is considered one subtype of variant AD. In PCA, a high consistency between the phospho-tau specific antibody

AT8 immunohistochemical staining and tau tracer binding was observed [33]. Tau-PET imaging showed significantly higher binding compared to patients with similar clinical features arising from dementia with Lewy bodies [34]. Patients with PCA presented with higher uptake in occipital and parietal brain regions, patients with amnesic-predominant presentation showed the highest binding in medial temporal and lateral temporoparietal regions[35]. Our data was consistently with the previous immunohistochemical and tau-PET studies.

We observed the strongest binding for the lentiform and thalamus both in AD and HC groups which might be largely associated with off-target binding. Off-target binding is a major limitation associated with the first-generation tau radioligands. In particular, the basal ganglia and thalamus were found to be affected by extensive binding to Monoamine oxidase B (MAO-B)[33,42].MAO-B is a flavoenzyme in the mitochondrial outer membrane and plays a major role in the metabolism of neuroactive and vasoactive amines. In the previous studies, the MAO-B binding was also considered as important off-target binding of THK probes. Previous study from Prof. Cui indicated that the [^{18}F]-S16 shared the same THK binding site of NFTs[16]. However, the parallel comparison between [^{18}F]-S16 and [^{18}F]-THK5351 revealed that S16 had many advantages such as high binding affinity, selectivity, initial brain uptake, and low off-target binding[16]. As such, there was lower [^{18}F]-S16 binding in the MAO-B rich lentiform in HCs than AD group in this study.

In this study, we directly compared the [^{18}F]-S16 SUVR and [^{18}F]-FDG SUVR for all cortical ROI regions in AD patients. Studies have shown a significant correlation between [^{18}F]-S16 binding and hypometabolism across neocortical regions. This finding was consistent with other tau radioligands PET studies[35-39]. The A/T/N classification scheme suggests that tau pathology follow in the time course of disease development after amyloid- β pathology. Early A β deposition occurs across much of the cortex even in clinically normal aging (e.g., preclinical AD), while tau pathology begins in the transentorhinal cortex in the MTL and may spread in an activity-dependent manner along vulnerable functional networks[32]. Animal studies have indeed shown the spread of tau pathology via synaptic connections, with this

process accompanied by neurodegenerative changes[40,41]. The tau protein plays a key role in the formation of intraneuronal NFTs and might represent an important therapeutic target in AD because tau deposition is highly associated with neurodegeneration and cognitive decline. Our findings clearly demonstrate that [^{18}F]-S16 PET can provide information on “T”. [^{18}F]-S16 tau PET imaging has the potential to facilitate accurate diagnosis of tauopathy, precise assessment of disease severity, disease progression, and efficacy of potential disease-modifying anti-tau treatments.

Conclusion

[^{18}F]-S16 could be automated synthesized on a large scale and it shows favorable biodistribution and safety to human body. The dosimetric data are comparable to other tau tracers. AD subjects show generally higher [^{18}F]-S16 uptake than HCs in cortical regions. And a significant correlation between [^{18}F]-S16 binding and hypometabolism across neocortical regions could be observed. We find prominent [^{18}F]-S16 uptake in regions where abnormal tau aggregates are expected to accumulate. Our results suggest that the new tau PET tracer is a suitable tool to distinguish AD and HCs. It is necessary to conduct more studies on more subjects and involve other tauopathies reactions.

DISCLOSURES

Funding This study was funded in part by the National Natural Science Foundation of China 82171982. Natural Science Foundation of Fujian 2020J05249. Fujian Provincial Health Commission Science and Technology and Programme 2020GGA045. Tianjin Education Commission Scientific Research Project (2018KJ060)

Conflict of interest The authors declare that they have no conflict of interest.

Acknowledgement The authors gratefully acknowledge Dr. Shuo Gao (Department of PET/CT Diagnostic, Tianjin Medical University General Hospital, Tianjin, China) for experimental design. In addition, we thank Yansheng Li, Hailei Yang and Biyao Hu for the technical assistance to this study.

KEY POINTS

QUESTION: Is the recently reported tau tracers [^{18}F]-S16 safe in healthy volunteers, and suitable for tau detection in AD patients?

PERTINENT FINDINGS:

We demonstrate the automatic synthesis of [^{18}F]-S16 and its favorable biodistribution and safety in healthy volunteers. AD subjects showed generally higher [^{18}F]-S16 uptake than HCs in cortical regions. And a significant correlation between [^{18}F]-S16 binding and hypometabolism across neocortical regions could be observed.

IMPLICATIONS FOR PATIENT CARE:

These results support prominent [^{18}F]-S16 uptake in regions where abnormal tau aggregates are expected to accumulate. [^{18}F]-S16 is a promising tracer for tauopathy diagnosis and provide opportunities of potential disease-modifying anti-tau treatments.

REFERENCES

- [1] Dani M, Wood M, Mizoguchi R, et al. Microglial activation correlates in vivo with both tau and amyloid in Alzheimer's disease. *Brain*. 2018; 141(9):2740-2754
- [2] Jack CR Jr, Bennett DA, Blennow K, et al. A/T/N: an unbiased descriptive classification scheme for Alzheimer disease biomarkers. *Neurology*. 2016; 87:539-547
- [3] Spire-Jones TL, Hyman BT. The intersection of amyloid beta and tau at synapses in Alzheimer's disease. *Neuron*. 2014; 82:756-771
- [4] Dani M, Edison P, Brooks DJ. Imaging biomarkers in tauopathies. *Parkinsonism Relat Disord*. 2016; 22:S26-S28
- [5] Fodero-Tavoletti MT, Okamura N, Furumoto S, et al. ¹⁸F-THK523: a novel in vivo tau imaging ligand for Alzheimer's disease. *Brain*. 2011; 134:1089-1100
- [6] Marquie M, Normandin MD, Vanderburg CR, et al. Validating novel tau positron emission tomography tracer [F-18]-AV-1451 (T807) on postmortem brain tissue. *Ann Neurol*. 2015; 78:787-800
- [7] Marquie M, Normandin MD, Meltzer AC, et al. Pathological correlations of [F-18]-AV-1451 imaging in non-alzheimer tauopathies. *Ann Neurol*. 2017; 81:117-128
- [8] Chien DT, Szardenings AK, Bahri S, et al. Early clinical PET imaging results with the novel PHF-tau radioligand [F18]-T808. *J Alz Dis*. 2014; 38:171-184
- [9] Walji AM, Hostetler ED, Selnick H, et al. Discovery of 6-(Fluoro-(18)F)-3-(1H-pyrrolo[2,3-c]pyridin-1-yl)isoquinolin-5-amine ([18F]-MK-6240): A Positron Emission Tomography (PET) Imaging Agent for Quantification of Neurofibrillary Tangles (NFTs). *J Med Chem*. 2016; 59:4778-4789
- [10] Betthausen TJ, Lao PH, Murali D, et al. In Vivo Comparison of Tau Radioligands ¹⁸F-THK-5351 and ¹⁸F-THK-5317. *J Nucl Med*. 2017; 58:996-1002
- [11] Hsiao IT, Lin KJ, Huang KL, et al. Biodistribution and Radiation Dosimetry for the Tau Tracer ¹⁸F-THK-5351 in Healthy Human Subjects. *J Nucl Med*. 2017; 58:1498-1503
- [12] Hashimoto H, Kawamura K, Igarashi N, et al. Radiosynthesis, Photoisomerization, Biodistribution, and Metabolite Analysis of ¹¹C-PBB3 as a Clinically Useful PET Probe for Imaging of Tau Pathology. *J Nucl Med*; 2014; 55:1532-1538
- [13] Kimura Y, Ichise M, Ito Hiroshi, et al. PET Quantification of Tau Pathology in Human Brain

with ^{11}C -PBB3. *J Nucl Med.* 2015; 56:1359-1365

- [14] Ni RQ, Ji B, Ono M, et al. Comparative in-vitro and in-vivo quantifications of pathological tau deposits and their association with neurodegeneration in tauopathy mouse models. *J Nucl Med.* 2018; 59(6):960-966
- [15] Betthausen T, Cody KA, Zammit MD, et al. In vivo characterization and quantification of neurofibrillary tau PET radioligand ^{18}F -MK-6240 in humans from Alzheimer's disease dementia to young controls. *J Nucl Med.* 2018; 60(1):93-99
- [16] Zhou KX, Yang F, Li YY, et al. Synthesis and Evaluation of Fluorine-18 Labeled 2-Phenylquinoxaline Derivatives as Potential Tau Imaging Agents. *Mol Pharm.* 2021; 18:1176-1195
- [17] Wang Y, Shi ZH, Zhang N, et al. Spatial Patterns of Hypometabolism and Amyloid Deposition in Variants of Alzheimer's Disease Corresponding to Brain Networks: a Prospective Cohort Study. *Mol Imaging Biol.* 2019, 21(1), 140-148
- [18] Zanotti-Fregonara P, Lammertsma AA, Innis RB. Suggested pathway to assess radiation safety of ^{18}F -labeled PET tracers for first-in-human studies. *Eur J Nucl Med Mol Imaging.* 2013; 40:1781-1783
- [19] Choi JY, Lyoo CH, Lee JH, et al. Human Radiation Dosimetry of [^{18}F]AV-1451(T807) to Detect Tau Pathology. *Mol Imaging Biol.* 2016; 18:479-482
- [20] Hsiao IT, Lin KJ, Huang KL, et al. Biodistribution and Radiation Dosimetry for the Tau Tracer ^{18}F -THK-5351 in Healthy Human Subjects. *J Nucl Med.* 2017; 58:1498-1503
- [21] Koole M, Lohith TG, Valentine JL, et al. Preclinical Safety Evaluation and Human Dosimetry of [^{18}F]MK-6240, a Novel PET Tracer for Imaging Neurofibrillary Tangles. *Mol Imaging Biol.* 2020; 22:173-180
- [22] Braak H, Braak E. Frequency of stages of Alzheimer-related lesions in different age categories. *Neurobiol Aging.* 1997; 18:351-357
- [23] Braak H, Alafuzoff I, Arzberger T, et al. Staging of Alzheimer disease-associated neurofibrillary pathology using paraffin sections and immunocytochemistry. *Acta Neuropathol (Berl).* 2006; 112:389-404

- [24] Ossenkoppele R, Rabinovici GD, Smith R, et al. Discriminative accuracy of [¹⁸F]flortaucipir positron emission tomography for Alzheimer disease vs other neurodegenerative disorders. *JAMA*. 2018; 320:1151-1162
- [25] Jack CR Jr, Wiste HJ, Schwarz CG, et al. Longitudinal tau PET in ageing and Alzheimer's disease. *Brain*. 2018; 141:1517-1528
- [26] Chiotis K, Saint-Aubert L, Savitcheva I, et al. Imaging in-vivo tau pathology in Alzheimer's disease with THK5317 PET in a multimodal paradigm. *Eur J Nucl Med Mol Imaging*. 2016; 43:1686-1699
- [27] Cho H, Choi JY, Hwang MS, et al. In vivo cortical spreading pattern of tau and amyloid in the Alzheimer disease spectrum. *Ann Neurol*. 2016; 80:247-258
- [28] Braak H, Thal DR, Ghebremedhin E, et al. Stages of the pathologic process in Alzheimer disease: age categories from 1 to 100 years. *J Neuropathol Exp Neurol*. 2011; 70:960-969
- [29] Tomlinson BE, Blessed G, Roth M. Observations on the brains of demented old people. *J Neurol Sci*. 1970; 11:205-242
- [30] Jellinger KA, Alafuzoff I, Attems J, et al. PART, a distinct tauopathy, different from classical sporadic Alzheimer disease. *Acta Neuropathol*. 2015;129:757-762
- [31] Josephs KA, Murray ME, Tosakulwong N, et al. Tau aggregation influences cognition and hippocampal atrophy in the absence of beta- amyloid: a clinico-imaging-pathological study of primary age- related tauopathy (PART). *Acta Neuropathol*. 2017; 133:705-715
- [32] Harrison TM, Maass A, Adams JN, et al. Tau deposition is associated with functional isolation of the hippocampus in aging. *Nat Commun*. 2019; 10(1):4900
- [33] Yap SY, Frias B, Wren MC, et al. Discriminatory ability of next-generation tau PET tracers for Alzheimer's disease. *Brain*. 2021; Epub ahead of print
- [34] Nedelska Z, Josephs KA, Graff-Radford J, et al: (18) F-AV-1451 uptake differs between dementia with lewy bodies and posterior cortical atrophy. *Mov Disord*. 2019; 34:344-352
- [35] Ossenkoppele R, Schonhaut DR, Schöll M, et al. Tau PET patterns mirror clinical and neuroanatomical variability in Alzheimer's disease. *Brain*; 2016;139(Pt 5):1551-1567.
- [36] Dronse J, Fliessbach K, Bischof GN, et al. In vivo patterns of tau pathology, amyloid-beta burden, and neuronal dysfunction in clinical variants of Alzheimer's disease. *J Alzheimers Dis*. 2017; 55:465-471

- [37] Ossenkoppele R, Schonhaut DR, Baker SL, et al. Tau, amyloid, and hypometabolism in a patient with posterior cortical atrophy. *Ann Neurol*. 2015; 77:338-342
- [38] Bischof GN, Jessen F, Fließbach K, et al. Impact of tau and amyloid burden on glucose metabolism in Alzheimer's disease. *Ann Clin Transl Neurol*. 2016; 3:934-939
- [39] Whitwell JL, Graff-Radford J, Tosakulwong N, et al. Imaging correlations of tau, amyloid, metabolism, and atrophy in typical and atypical Alzheimer's disease. *Alzheimer Dement*. 2018; 14(8):1005-1014
- [40] Ahmed Z, Cooper J, Murray TK, et al. A novel in vivo model of tau propagation with rapid and progressive neurofibrillary tangle pathology: the pattern of spread is determined by connectivity, not proximity. *Acta Neuropathol*. 2014; 127:667-683
- [41] de Calignon A, Polydoro M, Suarez-Calvet M, et al. Propagation of tau pathology in a model of early Alzheimer's disease. *Neuron*. 2012; 73:685-697

Figures

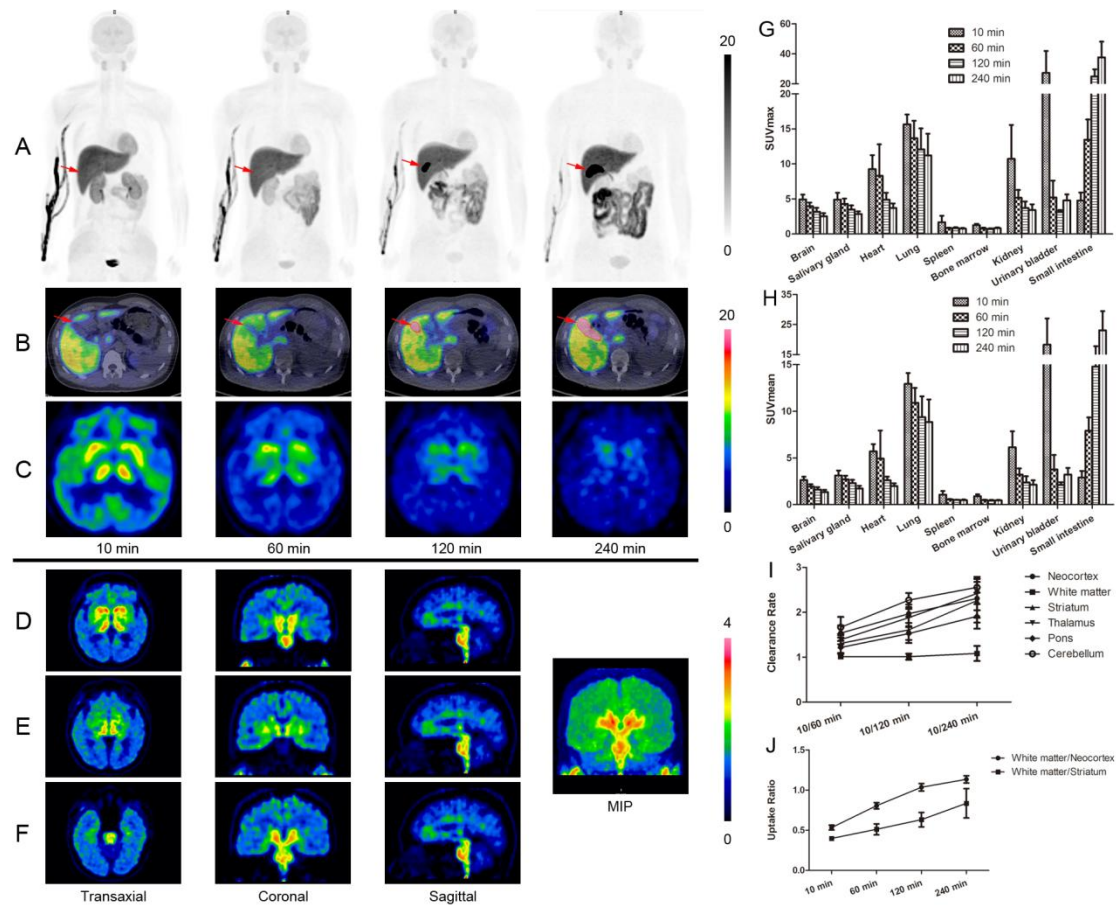


Figure 1. Whole-body PET images of $[^{18}\text{F}]\text{-S16}$ obtained in a healthy volunteer acquired over 8-bed positions of varying duration. The MIP images of $[^{18}\text{F}]\text{-S16}$ at 4 different time points after intravenous injection (A). The time-distribution pattern of $[^{18}\text{F}]\text{-S16}$ in the gall bladder (B, red arrow) and in the brain (C). Brain PET images obtained after the second whole-body scan approximately 76 minutes post-injection presented a transverse, coronal, and sagittal plane (D-F). SUV_{max} (G) and SUV_{mean} (H) value of $[^{18}\text{F}]\text{-S16}$ in main organs of healthy volunteers ($n = 4$) at 10, 60, 120 and 240 min post-injection. Brain clearance rate (10/60, 10/120, 10/240 min) (I), white matter/neocortex and white matter/striatum uptake ratio (10, 60, 120 and 240 min) (J) were summarized.

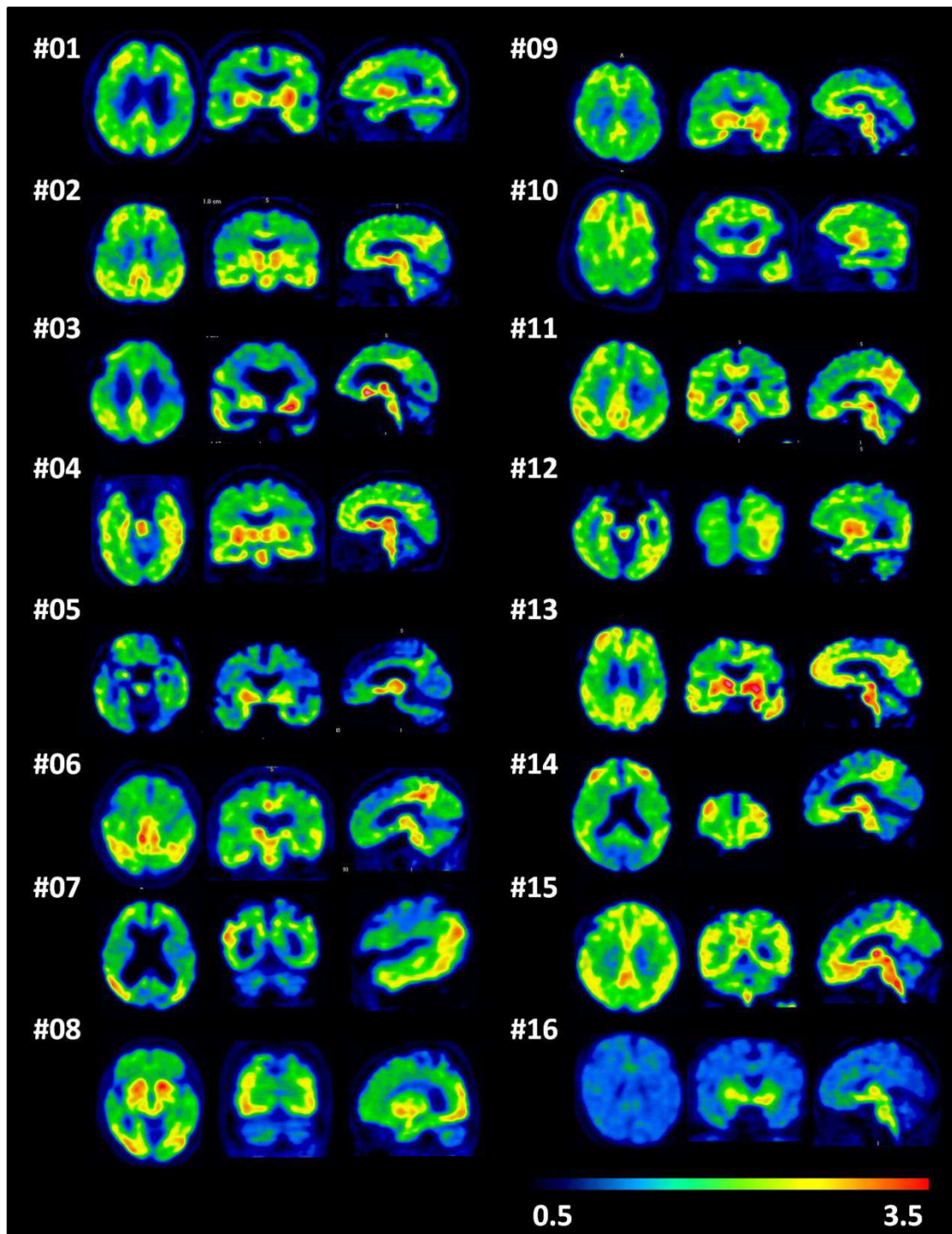


Figure 2. A single frame of [^{18}F]-S16 PET images (85-90 min) in a transverse, coronal, and sagittal plane for all AD patients (subjects#1-15) and one representative HC (subject#16).

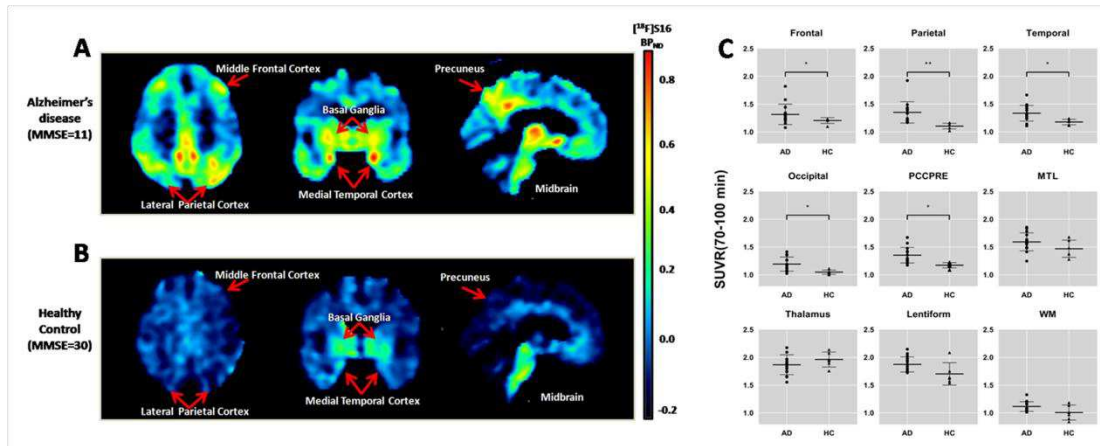


Figure 3. Comparison of a AD patient (subject#6, MMSE = 11) (A) and a HC (subject#16, MMSE = 30) (B) in the mean $[^{18}\text{F}]\text{-S16}$ BP_{ND} PET maps. Images were normalized to the MNI space and presented as a transverse, coronal, and sagittal plane. Box plot of SUVR (70-100 min) of each diagnosis group for different brain regions (C). Box plot of SUVR (70-100 min) at each diagnosis group for different brain regions. * $p < 0.05$. ** $p < 0.01$. *** $p < 0.001$. **** $p < 0.0001$.

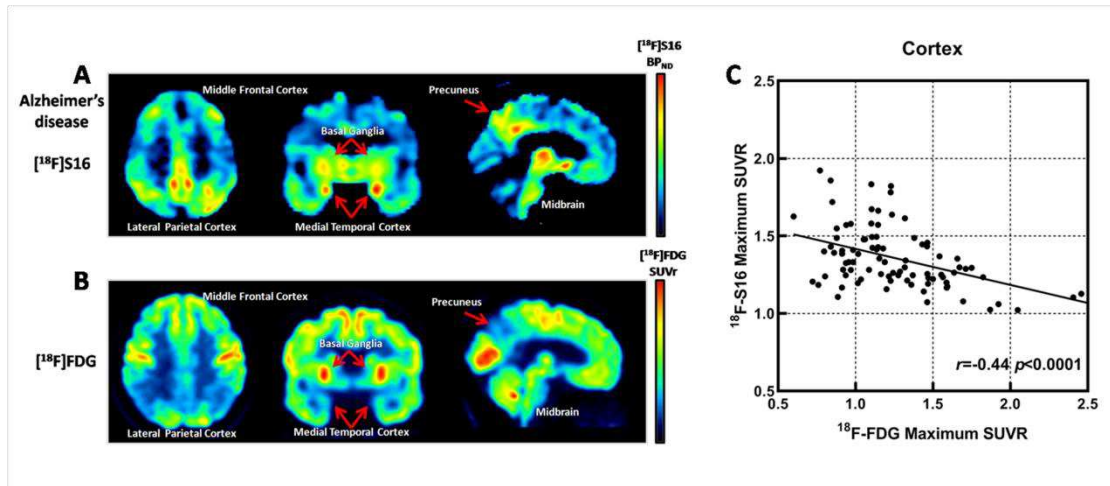


Figure 4. Comparison of $[^{18}\text{F}]\text{-S16 BP}_{\text{ND}}$ PET map and $[^{18}\text{F}]\text{-FDG SUVR}$ PET map obtained in same AD (subject#6). Images were normalized to the MNI space and presented as a transverse, coronal, and sagittal plane (**A&B**). Correlation plots for $[^{18}\text{F}]\text{-S16}$ and $[^{18}\text{F}]\text{-FDG}$ PET. $r = -0.44$, $p < 0.0001$ (**C**).

Tables

Table 1. Absorbed doses to target organs and effective dose

Target organs	Organ doses ($\mu\text{Gy}/\text{MBq}$)
Adrenals	17.0 ± 0.6
Brain	15.2 ± 1.0
Breasts	7.9 ± 0.3
Gallbladder wall	133.7 ± 60.9
Lower large intestine	11.8 ± 0.6
Small intestine	44.5 ± 5.4
Stomach wall	12.7 ± 0.2
Upper large intestine	18.9 ± 1.1
Heart wall	16.6 ± 0.7
Kidneys	31.6 ± 2.2
Liver	88.5 ± 11.2
Lungs	11.1 ± 0.2
Muscle	9.5 ± 0.3
Ovaries	13.7 ± 0.6
Pancreas	17.1 ± 0.6
Red marrow	11.3 ± 0.6
Osteogenic cells	11.7 ± 0.6
Skin	7.0 ± 0.3
Spleen	10.7 ± 0.3
Testes	7.7 ± 0.5
Thymus	9.2 ± 0.4
Thyroid	8.3 ± 0.5
Urinary bladder wall	10.6 ± 0.5
Uterus	13.2 ± 0.6
Parotid	14.3 ± 3.8
Total body	12.3 ± 0.1
Effective dose	15.3 ± 0.3

Table 2.Standardized uptake value ratios

ROI	AD	HCS
Frontal	1.32 (0.183)	1.21 (0.053)
Parietal	1.35 (0.192)	1.10 (0.050)
Temporal	1.33 (0.141)	1.18 (0.049)
Occipital	1.19 (0.127)	1.05 (0.039)
Posterior cingulate and precuneus	1.35 (0.141)	1.17 (0.048)
Medial temporal	1.59 (0.163)	1.47 (0.155)
Thalamus	1.87 (0.180)	1.96 (0.135)
Lentiform	1.88 (0.135)	1.70 (0.201)
White matter	1.12 (0.087)	1.01 (0.134)

AD: Alzheimer's disease; HCs: healthy controls; ROI: region of interest. Standardized uptake value ratios mean values (standard deviation) from 70 to 100 min using the cerebellar cortex as a reference region.

Supplementary Materials

Biodistribution and Dosimetry Evaluation for A Novel Tau Tracer [^{18}F]-S16 in Healthy Volunteers and Its Application in Assessment of Tau Pathology in Alzheimer's Disease

Ying Wang¹, Li Cai¹, Kaixiang Zhou², Mengchao Cui², Shaobo Yao^{1,3*}

¹ Department of PET/CT Diagnostic, Tianjin Medical University General Hospital, Tianjin, 300052, China

² Key Laboratory of Radiopharmaceuticals, Ministry of Education, Beijing Normal University, Beijing, 100875, China

³ Department of Nuclear Medicine, Fujian Provincial Key Laboratory of Precision Medicine for Cancer, The First Affiliated Hospital of Fujian Medical University, Fuzhou, Fujian, 350005, China

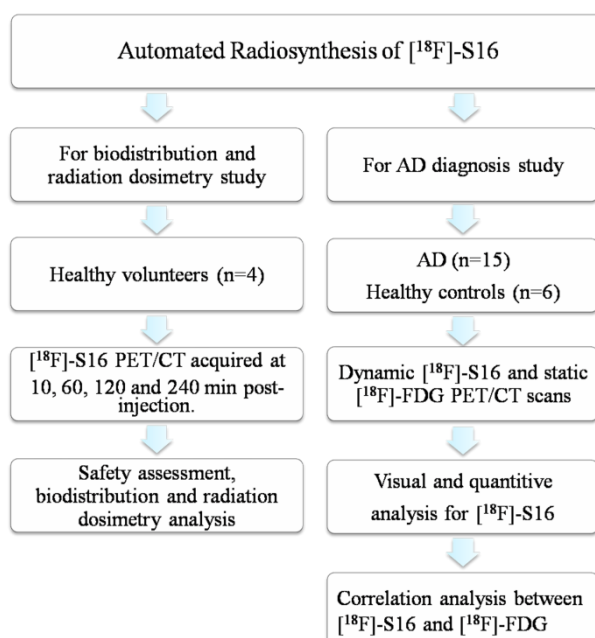


Fig. S1 The flowchart of study design. The automated radiosynthesis of [^{18}F]-S16 was performed. And then four healthy volunteers were underwent a series PET scans acquired at 10, 60, 120 and 240 min post-injection. The biodistribution in normal organs and safety were assessed. Radiation

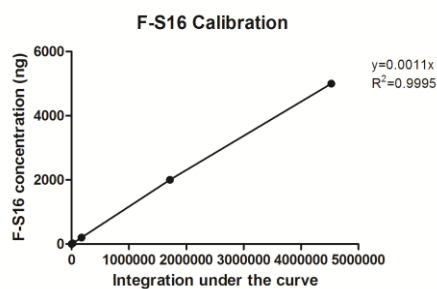


Fig. S4 With an integration of 5157 (area under the curve), the concentratio of [^{18}F]-S16 (referred to as F-S16 in the graph) 5.7 ng. The overall specific activity was determined to be 1480 GBq/ μmol . The average specific activity 1047 ± 450 GBq/ μmol for synthesis ranging from 30-37 GBq of n.c.a [^{18}F]-Fluoride as starting activity

Table S1. Demographic and clinical characteristics of participants

Subject NO.	Gender	Age(y)	Cohort	Injected dose (MBq)	Amyloid Status (visual)	MMSE Score	CDR Score
1	Male	68	AD	399.6	Positive	21	1
2	Male	54	AD	384.8	Positive	18	1
3	Female	71	AD	362.6	Positive	20	0.5
4	Male	77	AD	329.3	Positive	19	0.5
5	Female	54	AD	373.7	Positive	21	0.5
6	Female	55	AD	340.4	Positive	11	2
7	Female	64	AD	414.4	Positive	15	1
8	Female	60	AD	418.1	Positive	19	1
9	Male	68	AD	377.4	Positive	26	0.5
10	Male	57	AD	444.0	Positive	10	2
11	Female	41	AD	384.8	Positive	25	0.5
12	Male	64	AD	395.9	Positive	11	1.5
13	Female	79	AD	444.0	Positive	23	0.5
14	Female	57	AD	370.0	Positive	14	1
15	Female	66	AD	329.3	Positive	27	0.5
16	Female	56	HC	388.5	Negative	30	0

Subject NO.	Gender	Age(y)	Cohort	Injected dose (MBq)	Amyloid Status (visual)	MMSE Score	CDR Score
17	Female	61	HC	373.7	Negative	30	0
18	Male	63	HC	381.1	Negative	30	0
19	Female	72	HC	381.1	Negative	29	0
20	Female	60	HC	370.0	Negative	30	0
21	Male	55	HC	392.2	Negative	30	0

In total, 15 AD subjects and 6 HCs were included in this analysis. Subject demographics and clinical characteristics are presented in Table 1. Mean age was 62.3 ± 9.9 for AD subjects and was 61.2 ± 6.1 for HCs. There were no significant differences in age and gender ($p > 0.05$). Mean MMSE scores in the AD and HCs groups were 18.6 (range, 10-27) and 29.8 (range, 29-30). Mean CDR scores in the AD and HCs groups were 1.0 (range, 0.5-2.0) and 0. MMSE score and CDR score in the HCs group were higher than AD group ($p < 0.05$). The amyloid status were positive in AD group and were negative in HC group by visual assignment.)